Far-field far-subwavelength spatial resolution using relative motion with structured illumination

Justin A. Patel ◉, Christopher M. Lacny ◉, Vivek Raghuram ◉, and Kevin J. Webb ◉*

School of Electrical and Computer Engineering, Purdue University, West Lafayette, Indiana 47907-2035, USA

Relative motion of structured optical illumination with respect to an object and far-field measurement of intensity are presented as a means to obtain far-subwavelength spatial resolution with a direct imaging arrangement. The principle behind this approach is that the variable interaction of an object with a background field generates information about nanometer-scale features that is encoded in the propagating plane-wave spectrum, allowing far-field data that are modulated with motion according to the nanostructure. Information theory supports this superresolution mechanism and illustrates sensitivity with respect to the illumination and detection arrangements. Simulations indicate that available lasers and detectors would enable a resolution of $\lambda/1000$ with modest signal-to-noise requirements and single-pixel detection. Relative motion in structured fields is shown to enhance spatial resolution achievable using data inversion with constraints. Importantly, far-subwavelength sensitivity is shown to be achievable even when the illuminating field is unknown. These results suggest applications that include material defect detection and unlabeled protein sensing, and direct extensions to estimating geometrical features at unprecedented spatial resolution become possible.

I. INTRODUCTION

Achieving high lateral spatial resolution is critical in science and technology, and the infrared through ultraviolet wavelength range is of great importance for innumerable domains. A common physical measure is distinguishing the separation between two small objects, two apertures, for example. The Abbe diffraction limit constrains conventional far-field imaging methods to a maximum achievable resolution of $\lambda/2n$, with λ being the free-space wavelength and n the refractive index of the background medium. This can loosely be understood by loss of the evanescent field portion of the plane-wave spectrum, leaving the propagating spectrum. Significant scientific insights and technological developments are locked behind this link between wavelength and resolution. We present the physical basis for achieving virtually unlimited spatial resolution using relative motion in structured illumination, where either the object or the field is scanned and far-field intensity measurements are made. In this situation, relative motion between the field and the object encodes nanostructure information in the propagating plane waves, allowing intensity measurements to be sensitive to far-subwavelength transverse geometries. In an experiment using a laser, nanometer-scale object features should be resolvable without the need for fluorescent labeling. In the examples presented, an interfering beam and speckle fields are considered, with a view to implementation strategies and the possible suite of applications.

One approach to access high-spatial-frequency information is near-field scanning of a tip (to directly measure or scatter). However, such methods may not be practically feasible, and they are generally slow and obtrusive. Another method makes use of structured illumination and moiré fringes and grants an increase in resolution by a factor of two by extending the range of spatial frequencies that can be accessed [1,2], an approach that is known as structured illumination microscopy (SIM). It has also been established that random speckle fields can be used to access this factor of two in resolution improvement without the requirement of knowing the fields [3]. Structured fields are also the basis of a nanometer-scale optical ruler using a Pancharatnam-Berry phase metasurface, where singularities can be revealed with interferometry [4].

In quantum optics, the twofold de Broglie wavelength reduction of entangled photon pairs [5], relative to that for the individual photons, can be, in principle, extended to a larger number of photons. Exploiting this in practice requires a commensurate multiphoton detection method. However, the spatial resolution is that associated with the total energy, and hence the parent photon. Higher-order photon-counting correlations, in a configuration that extends the Hanbury Brown–Twiss interferometer measurement from two detectors, provide opportunities for higher spatial resolution with the observation of multiphoton interference patterns from statistically independent light sources [6,7]. In fluorescence microscopy, higher-order photon correlations have been presented as a means to reduce the width of the point spread function of a microscope [8,9], offering an avenue for improved spatial resolution. By combining structured illumination with these higher-order correlations, an even greater resolution enhancement has been shown for quantum emitters [10].

In the biosciences, fluorescent labeling has become pervasive as a means to obtain information through various forms of microscopy, such as fluorescent lifetime imaging microscopy (FLIM). At the single-molecule level, fluctuation correlation spectroscopy (FCS) has been commonly used [11].

*webb@purdue.edu

023509-1

Importantly, with the constraint of the point spread function of a microscope and, when it is possible to ascribe a single point emitter in space, that point can be located to a precision far greater than the visible wavelengths used in microscopy. For example, fluorescence-based techniques such as stimulated emission depletion microscopy (STED), photoactivated localization microscopy (PALM), and stochastic optical reconstruction microscopy (STORM) demonstrate subwavelength resolution [12–14]. While these techniques extract the equivalent point location of a fluorophore, this may or may not provide underlying information on the host material, a cell, for example, and fluorescent labeling is not always desirable or feasible.

Single-pixel imaging encompasses a range of techniques for reconstructing the scene with a single-pixel camera. This is accomplished through spatial modulation of either the illumination or detection light [15]. Reconstruction using these measurements is done with the addition of prior information of some kind, for example, within a compressed sensing framework [16] or with the use of machine learning [17].

Relative motion has been used in various imaging approaches that do not access subwavelength spatial information. In x-ray microscopy, relative motion between the beam and the specimen forms the basis of multiple techniques, such as scanning transmission x-ray microscopy [18] or x-ray ptychography [19]. Ptychography recovers an image of the specimen by measuring diffraction patterns that occur when the coherent beam and specimen are moved relative to each other. The computational inversion process uses a phase-retrieval method that requires significant overlap of these relative positions [20]. Ptychography has been used to image weakly scattering specimens, such as biological samples [21]. "Superresolution" methods from digital image processing [22] have been used to increase the resolution of obtained ptychographic images [23]; it should be noted that this usage of the term "superresolution" is in the context of image processing and exploits subpixel shifts during acquisition, and it does not imply breaking the Abbe limit.

Prior simulation studies have demonstrated sensitivity to far-subwavelength object features using relative motion in structured illumination [24,25]. These studies consider object motion relative to a known, deterministic illumination pattern and demonstrate sensitivity to changes in feature geometry on the order of $\lambda/100$. Additionally, these results rely either partially [24] or completely [25] on information from detectors that are perpendicular to the plane of the object feature of interest and thus provide high sensitivity due to phase differences between scatter from different parts of the object at the detector plane. The direct imaging arrangement, where the object lies in a plane parallel to the detector, is important in microscopy because it allows the straightforward use of lens systems to focus light, and limits the deleterious effect of optical scatter from the object (see Ref. [26], for example: p. 281 for an introduction to the microscope and pp. 465–471 for the resolving power of a microscope and the Abbe limit). Almost all common methods in optical microscopy utilize this arrangement. Thus, further analysis that considers the direct imaging arrangement is of substantial practical interest. Fundamentally, these studies demonstrate that far-subwavelength object information can be encoded in
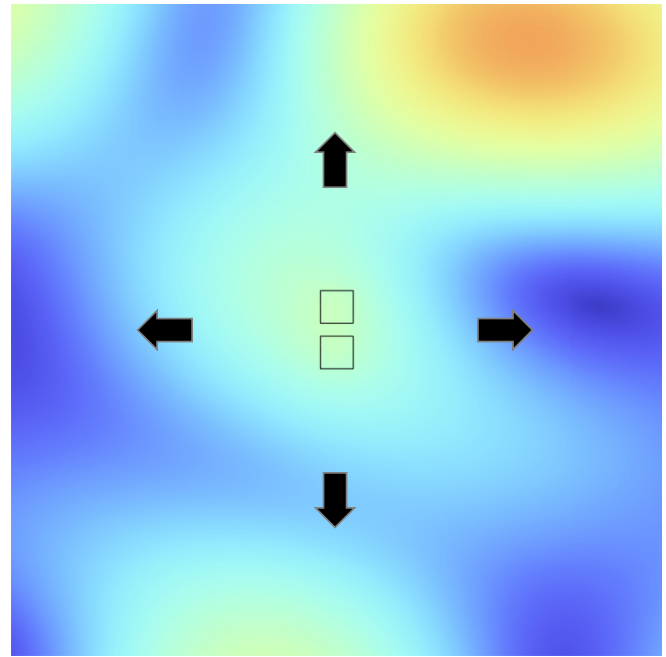

FIG. 1. Concept figure showing relative motion between an object and a structured electric field. The object could be stationary in a translated field, as is primarily considered in this work, or vice versa. An example speckle field is shown in this case, for a subset of the simulation region, although other types of illumination are possible. The figure is to scale with regard to the object size in relation to the fully developed speckle having half-wavelength spatial correlation (speckle size).

the propagating plane-wave spectrum and measured in the far-field. However, the roles of relative motion in structured illumination, measurement geometry, prior information, and multiple scatter in encoding this information have not been completely understood.

We present the physical basis for achieving far-subwavelength spatial resolution in a direct imaging configuration using far-field intensity data and either motion of an incident structured field over an object or motion of the object in a background field. Information theory provides an understanding of the underlying phenomena that allow access to nanostructure information with visible laser light. Our results clarify the role of relative motion in structured illumination, interferometric information due to the geometry of the object and detector, prior information, and multiple scatter in achieving high spatial resolution. The arrangement considered in a set of simulations is illustrated in Fig. 1. The field could be scanned by various means, including the use of a spatial light modulator. The object may also be scanned in space, such as with a piezoelectric transducer [24]. Changes in optical intensity are measured in the far field as these relative positions change, and these measurements are sensitive to far-subwavelength changes in the object's geometry. Numerical simulations and information theory support the opportunity spaces presented. Far-subwavelength sensitivity is possible, even if no forward model is available to connect these geometric changes and intensity measurements, i.e., when the incident field is unknown. However, if such a forward model

does exist, then it can be used for inversion with suitable constraints.

Simulation results are presented in Secs. II and III, and these provide the underpinnings of the physical contributions of this work. In the first situation considered (Sec. II), two plane waves are incident perpendicular to one another to provide the structured field, and relative motion in this field is shown to allow superresolution sensing in an imaging arrangement. In the second arrangement (Sec. III), a speckle field is used, as would occur with laser light passing through a randomly scattering material, being representative of an important class of problems involving randomly scattering media, and relative motion with respect to an object investigated. Because the power is integrated over multiple detector points, the metric is one involving single-pixel detection with a fixed aperture. In more detail and of direct relevance to the key contributions, Secs. II A–II C introduce the simulation and noise models; the results in Sec. II D provide insight into the physical problem, as well as demonstrating the rough equivalence of field and object motion for superresolution; Sec. II E quantifies the available resolution with this technique and provides insight into the role of signal-to-noise ratio (SNR) and measurement geometry in achieving far-subwavelength resolution. Section III provides insight into the role of prior information about the field and object, demonstrating that sensitivity to nanoscale features exists even when random speckle illumination is used. Section IV discusses various aspects of the work and the broader implications. Following the conclusion in Sec. V, where the contributions of this work are summarized, Appendices A through C cover numerical accuracy of the simulations, experimental achievability of the required sensitivity, and a proposed experimental implementation.

II. PLANE-WAVE ILLUMINATION

A. Simulation setup

We consider numerical field solutions for the two-dimensional (2D) measurement arrangement in Fig. 2(a), where the task is to resolve the separation D between two square dielectric rods, each with a dielectric constant of ϵ_r and 0.05λ on a side, shown in an expanded view in Fig. 2(b). The finite element method (FEM) [27] is used to solve for the scattered electric field in the temporal Fourier domain. To solve for the scattered fields, the domain is bounded by a 2λ-thick perfectly matched layer (PML) on all sides to simulate unbounded space. The total electric field is formed as the superposition of this scattered field solution and the prescribed structured incident field, and the magnetic field is subsequently determined. The FEM mesh is configured as described in Appendix A.

The structured background field consists of two plane waves of the same frequency (circular frequency ω), propagating perpendicularly to each other. With $\exp(j\omega t)$ dependence, we have the electric field

$$\mathbf{E} = \{e^{-j(k_0 x + \phi_x)} + e^{-j(k_0 y + \phi_y)}\}\hat{\mathbf{z}}, \tag{1}$$

where $k_0 = 2\pi/\lambda$ is the free-space wave number, and ϕ_x and ϕ_y are phases that are regulated to scan the interference fringes over the object.
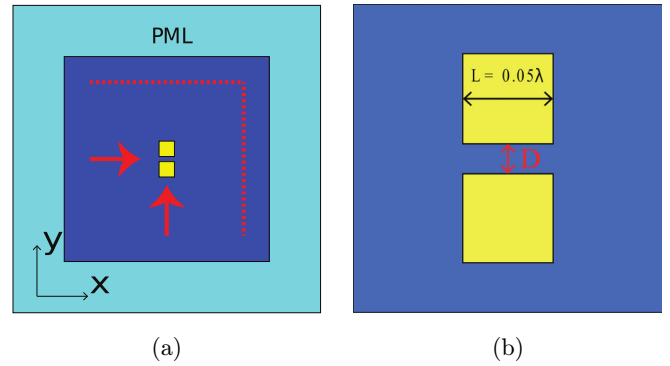

FIG. 2. (a) The free-space simulation domain is a square 6λ on a side and bounded by a 2λ-thick PML on all sides. Two dielectric scatterers are placed in the center, forming an object with separation D to be resolved. The red arrows indicate the direction of propagation of the incident plane waves. The dotted red lines represent the detector arrays, which measure the normal component of the time-average Poynting vector (intensity). (b) The central region is enlarged to show the scatterers of side $L = 0.05\lambda$ and separation D. These figures are not drawn to scale, in that the object size is larger than that used in the simulations, given the detector arrangement presented (with this size of the objects, the detectors would be located farther away than shown).

Two perpendicular detector planes (lines in the 2D simulations) are used, as indicated by the (red) dotted lines in Fig. 2(a), and the power flow determined by the integral of the normal component of the time-averaged Poynting vector ($\mathbf{S} = \mathrm{Re}\{\mathbf{E} \times \mathbf{H}^*\}/2$), with Re being the real part and $\mathbf{H}$ the phasor magnetic-field intensity. The Poynting vector is based on the total field (background plus scattered). By determining the power flow at a set of points in the detector plane, we simulate power flow through a series of small apertures, such as those corresponding to camera pixels. Due to the use of the integral of this power flow over the detector planes, we consider this data to be fundamentally single-pixel. These detection points are sufficiently far from the object (2.5λ from the centerlines of the binary object in question) so as to consider the intensity data to be in the far field with respect to the evanescent fields. Since the evanescent fields are negligible at the detectors, similar results could be achieved with the detector planes positioned much farther from the objects, so long as a similar solid angle of light is collected. As a result, this setup could be accomplished in an experiment using macroscopic optics that direct the scattered light into a single detector. The compact simulation domain is used to ensure tractable simulation times. Each array of detectors is placed a distance $\lambda/2$ from the nearest boundary. Based on the FEM mesh density, our simulation generates 503 uniformly spaced intensity-detection points along each detector array at which the time-averaged Poynting vector is calculated.

Although the primary focus of this paper is on lateral resolution (corresponding to the right detector plane in these simulations), the top detector plane is included in order to allow straightforward comparison with prior literature [24] and to assess the role of measurement geometry in resolution. Results presented in Sec. II D integrate data from both detector planes in order to appraise the overall sensitivity of

the measurement and demonstrate the equivalence of field and object motion, while results in Sec. II E are broken down between the two detector planes in order to demonstrate the role of measurement geometry and provide a clear metric for lateral resolution.

B. Noise model

Independent additive noise at the set of point detectors along the two orthogonal detector lines [Fig. 2(a)] is simulated by using a zero-mean Gaussian density function whose standard deviation (σ_s) is proportional to the time-averaged Poynting vector ($S_d = \hat{\mathbf{n}} \cdot \mathbf{S}$, where $\hat{\mathbf{n}}$ is the perpendicular unit vector to the detector line in a direction for $S_d > 0$) detected at that point. The SNR defines σ_s through $\sigma_s = S_d/\text{SNR}$. This fixed-SNR noise model is a computationally simple one meant to facilitate a proof of concept and allow convenient comparison with related literature. Here, a conservative SNR of 40 dB is assumed [24] (see Appendix B) for the intensity-detection points, giving $\sigma_s = 10^{-4}S_d$. Taking into account the 1006 such points adds approximately 14.1 dB when considering a measurement over the entire detector, so that the SNR for the final measurement becomes about 54.1 dB. From here onward, all SNRs discussed in this section will include this additional 14.1 dB.

This fixed-SNR additive Gaussian noise model is practically equivalent to both a high-count shot-noise model and a thermal noise model at the same SNR for these simulations. The scattered field measured at each detector plane is small relative to the incident field, so the power flow through the detectors varies little with D, ϵ_r, ϕ_x, and ϕ_y ($<0.1\%$). As a result, the SNR would vary little between measurements under a thermal or shot-noise model. The fixed-SNR model is therefore a good approximation of both noise models. In the strong-signal regime, the Poisson statistics of shot noise converge to a Gaussian distribution with standard deviation proportional to $\sqrt{N}$, where N is the number of detected photons.

Our simulations model a bright-field measurement, resulting in significant power-flow through the detector; thus, the use of an additive Gaussian noise model [28,29] is appropriate, even if the measurement is shot-noise limited. Under a shot-noise model, the SNR of 54.1 dB used in much of this analysis corresponds to 13.2 nW of optical power flowing through the detector planes, assuming an integration time of 1 s and a wavelength of 1 μm. This level of power density in the incident field is reasonable for a focused laser source, and single-photon detectors that are essentially shot-noise limited are widely available. As a result, the chosen SNR of 54.1 dB could be comfortably achieved in an experimental realization of this work.

C. Visualization and forward model

To demonstrate sensitivity to a change of 0.01λ in D, we compare noisy data obtained for each value of D, here $D = 0.01\lambda$ and 0.03λ, with the noiseless data for the reference $D = D_0 = 0.02\lambda$, for both the object-motion and the field-scanning scenarios. Data correspond to the difference in the total power flow through both detector arrays for an ordered

pair of parameters (p_x, p_y) relative to their initial values (0,0). In the field-scanning case, the parameters correspond to the change in the phases of the incident waves, ($\Delta\phi_x$, $\Delta\phi_y$). For object motion, (p_x, p_y) corresponds to the position translation of the object given by (Δx, Δy). The sensitivity is calculated using the measure

$$f(p_x, p_y; D) = \int [\mathbf{S}(x, y; p_x, p_y, D) - \mathbf{S}(x, y; 0, 0, D)] \cdot \hat{\mathbf{n}}\, ds \tag{2}$$

as the difference in the total power flow obtained by integrating $\mathbf{S}$ along both detector arrays for every (p_x, p_y), relative to that for the reference value (0,0). When noise is added to the Poynting vector, $\mathbf{S} \rightarrow \mathbf{S}_n$ [so, $f \rightarrow f_n$]. To highlight the measurable difference in data between two different separations, D and D_0, we define the function

$$g(p_x, p_y; D) = f_n(p_x, p_y; D) - f(p_x, p_y; D_0). \tag{3}$$

In the remainder of this paper, g_s is used to refer to this function in the case where a structured plane-wave field is translated over an object [as in (1)], g_m is used to denote object motion in a structured plane-wave field, and g_p is used to denote translation of a speckle field over an object. The integration in (2) and any averaging performed with noisy data to calculate $f_n(p_x, p_y; D)$ are commutable. As mentioned in Sec. II B, calculating $g(p_x, p_y; D)$ using power flow measurements from multiple noisy detectors is therefore equivalent to doing so from the power flow through a single detector, although the summation over noisy measurements in (2) for f_n has the effect of partly mitigating the noise because it is a sum over independent Gaussian random variables.

Care should be taken when considering the implications of (2) and (3). Equation (2) describes the measured power through a detector for a given type of object and its relative position with the field. It does not involve any comparison with a model; it only compares these measurements with each other (specifically, to a reference position). Therefore, $f(p_x, p_y; D)$ describes how the measured power changes as the relative positions change. This contains the core mechanism for far-subwavelength sensitivity that this paper describes, as it will be shown that $f_n(p_x, p_y; D)$ is sensitive to small changes in D (for a structured field). Equation (3) incorporates a noiseless version $f(p_x, p_y; D)$, which is computed with a model. This noiseless computed data is subtracted from the noisy experimental version, but this is done only for the purpose of visualizing how (2) changes with D. The symmetry of $g(p_x, p_y; D)$ can be seen in Figs. 3–5.

D. Structured illumination results

Figure 3 shows the first in a series of simulations that appraise the resolution of the method. The field is scanned by varying $\Delta\phi_x$ while $\Delta\phi_y = 0$, the object is fixed at the origin, as in Fig. 2, and the resulting $g_s(\Delta\phi_x, \Delta\phi_y; D)$ is plotted in Fig. 3. The error bars are generated empirically by using 100 sets of noisy Poynting vector data and a SNR of 40 dB at each of the intensity-detection points, for a final SNR of 54.1 dB after taking into account all such points (see Sec. II B). The length of the error bars is twice the standard error in estimating the mean value of g_s. A reference value of $D_0 = 0.02\lambda$ is

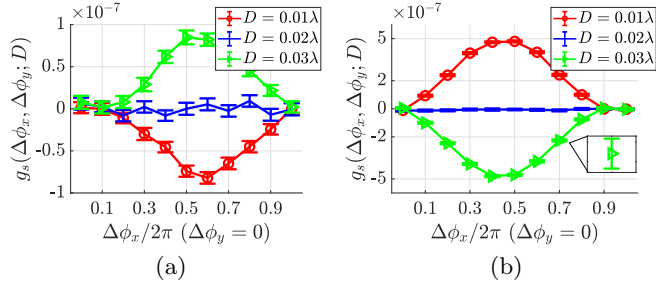(a)   (b)

FIG. 3. Resolution performance for the arrangement in Fig. 2 with phase scanning of the structured field described by (1). The reference separation is $D_0 = 0.02\lambda$. The object in panel (a) has $\epsilon_r = 1.5$ and in panel (b) has $\epsilon_r = 4$. The error bars are generated empirically using a SNR of 54.1 dB. Separation changes of 0.01λ are easily distinguished with far-field data. When ϵ_r is increased, this distinguishability increases as well.

used, referring to (3). The object is subject to the complete range of the 2π-periodic background electric field, with differences in D being captured by g_s. The dielectric constant is varied, with Fig. 3(a) showing $\epsilon_r = 1.5$ and Fig. 3(b) showing $\epsilon_r = 4$. At each position of the scatterers, the error bars are negligible relative to the features in g_s, showing that a change of 0.01λ in D can be easily resolved. The larger dielectric contrast in Fig. 3(b) results in more pronounced variations in g_s, both in absolute terms and also with respect to the error bars. The curves approach zero near $\Delta\phi_x/2\pi = 0$ because of the subtraction in (2), and near $\Delta\phi_x/2\pi = 1$ because of the periodicity of the illumination. More details are given in Appendix B.

Figure 4 shows a similar simulation, but with a moving object and stationary field instead. The object is scanned along a line parallel to the y axis, while fixing $\Delta x = -0.5\lambda$. In these results, ($\Delta x = 0$, $\Delta y = 0$) corresponds to the center of the simulation area, where the scatterers are positioned in the field scanning simulations. All other aspects of the simulation are similar to Fig. 3. The dielectric constant is again varied, with Fig. 4(a) showing results for $\epsilon_r = 1.5$ and Fig. 4(b) those for $\epsilon_r = 4$. Although the shape of the curves changes compared with Fig. 3, the general conclusions remain the same regarding spatial resolution and separability as ϵ_r is varied. We thus
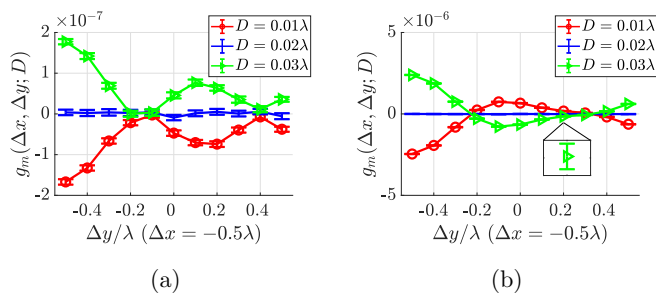

(a)   (b)

FIG. 4. Resolution performance with a stationary field and moving object are used for comparison with Fig. 3. Δy is varied in steps of 0.1λ from -0.5λ to 0.5λ, while Δx is fixed at -0.5λ. As in Fig. 3, the object for panel (a) has $\epsilon_r = 1.5$ and for panel (b) has $\epsilon_r = 4$. Despite the different shapes of the curves, it is still the case that the separation between the curves increases with ϵ_r.
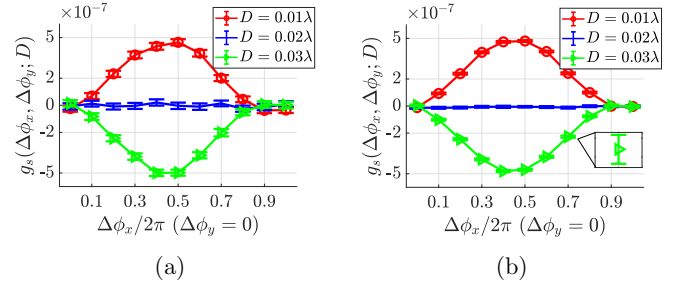

(a)   (b)

FIG. 5. Effect of detector noise for the arrangement in Fig. 2 with phase scanning of the field and $\epsilon_r = 4$. The error bars are generated using a SNR of (a) 49.1 dB and (b) 54.1 dB. Other simulation parameters are similar to those of Fig. 3. The relationship between SNR and distinguishability is explored further in Sec. II E.

conclude that object motion over short distances and field scanning are roughly equivalent for superresolution.

Figure 5 explores the effect of varying detector SNR on the distinguishability of the different values of D. A 49.1-dB SNR is shown in Fig. 5(a), compared with the 54.1-dB SNR in Fig. 5(b). Note that Figs. 3(b) and 5(b) show the same data; it is reproduced here for easier comparison. A lower SNR results in a diminished ability to sense the small gap but changes much less than $\lambda/100$ can still be detected, demonstrating the robustness of the technique to increased noise.

E. Information theory analysis (field motion)

Information theory provides a measure by which one can estimate the achievable resolution with given experimental parameters and more rigorously quantify the resolution achievable with the measurement configuration explored in the previous sections. While we now understand that nanostructure information is available in the far field with relative motion in structured illumination, we have yet to appraise how far we might expect to move into the subwavelength domain, beyond estimates from the examples in Figs. 3–5. With reference to the object and detector arrangement in Fig. 2(a), we use information theory to investigate the trend with reducing separation between the objects and the relative importance of the x detector [on the right in Fig. 2(a)] and the y detector (on the top).

The Cramér-Rao lower bound (CRB) for the variance of an estimate of scatterer separation from a measurement of the power flow through the detector planes is computed as a resolution measure. In general, the CRB is the minimum variance of an unbiased estimator of an unknown parameter from a random variable with a distribution which depends on that parameter. It bounds the performance of inversion techniques [30], such as the cost-function approach explored in Sec. II F. Computing the CRB provides a more quantitative metric to complement the physical insight provided by the curves shown in Figs. 3–5, and also yields information about which field and detector plane positions provide the most sensitivity to scatterer separation.

This analysis considers the case of field motion with the field and object geometries introduced in Sec. II A. Using the same fixed-SNR Gaussian noise model described in Sec. II B, we can express the likelihood function of a measurement

of the power flow through the detector at N incident-field positions, representing N values of $(\Delta\phi_x, \Delta\phi_y)$, as

$$p(\mathbf{m}, D) = \prod_{i=1}^{N} \frac{1}{\sqrt{2\pi\sigma_i^2}} \exp\left[-\frac{1}{2\sigma_i^2}(m_i - P_i(D))^2\right], \quad (4)$$

where $\mathbf{m}$ is a vector of power flow measurements through the detector, P_i is the noise-free power flow through the detector (with elements m_i) at field position i computed from the numerical field simulations, and σ_i is the standard deviation of the power flow measurement at field position i which, with the chosen fixed SNR noise model, is equal to $P_i/$SNR. The Fisher information, which represents the sensitivity to D provided by each measurement, is given by [30]

$$I(D) = -E\left[\frac{\partial^2 \ln p(\mathbf{m}, D)}{\partial D^2}\right], \quad (5)$$

with $E[\cdot]$ being the expected value. The CRB can be computed from the Fisher information using

$$\sigma_{\hat{D}}^2 = \mathrm{var}(\hat{D}) \geqslant \frac{1}{I(D)}, \quad (6)$$

where $\hat{D}$ is an unbiased estimate of the true value of D.

1. Cramér-Rao lower bound for structured illumination

Numerical data for the power flow through the detector [see Fig. 2(a)] are computed for values of D between 0λ and 0.03λ in increments of 0.001λ with scanned structured illumination. These data are used to determine the Fisher information and Cramér-Rao lower bound for estimating D. Data are collected for 11 evenly spaced values of $\Delta\phi_y$ between 0 and 2π. The CRB calculation assumes that these 11 measurements are used together to estimate D. The analysis is performed with $\epsilon_r = 4$, and ϵ_r is assumed to be known when computing the CRB for D. This is done in order to ascertain the sensitivity of the measurement to separation alone, providing a lower bound on the potential spatial resolution achievable with the measurement configuration explored in Sec. II. If the dielectric constant is unknown, and a two-parameter inversion must be performed, then the achievable resolution will be reduced. An analysis of the two-parameter inversion problem could be performed using a similar approach.

Figure 6(a) shows the square root of the CRB for estimating D ($\sigma_{\hat{D}}$) from a measurement of the power flow through the combined detector plane [top and right dashed line in Fig. 2(a)] at each value of $\Delta\phi_y$ as a function of D with a 54.1-dB SNR. This metric represents the minimum achievable standard deviation for an estimate of scatterer separation from this measurement, and doubling this value provides a sound statistical measure for resolution. Three curves are shown in Fig. 6(a), one assuming that only the top detector plane in Fig. 2 (referred to here as the y detector plane) is used, one assuming that only the right detector plane (the x detector plane) is used, and one where the sum of the power flow through both detector planes is measured. Since the combined detector plane collects roughly double the optical power of the individual (x and y) detector planes, a measurement with the combined detector should produce a higher SNR. This can be considered in the context of a shot-noise picture, where the
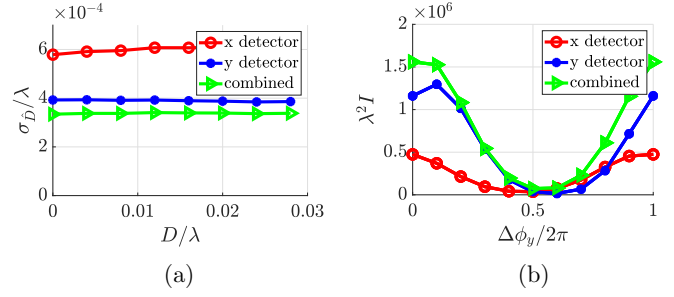

FIG. 6. Cramér-Rao bound and Fisher information for estimating D from power flow through the detector plane, scaled in terms of λ. $\epsilon_r = 4$ for both panels. (a) Square root of the CRB variance of $\hat{D}$ as a function of D for three detector plane configurations using data corresponding to 11 values of $\Delta\phi_y$. (b) Fisher information as a function of $\Delta\phi_y$ for three detector plane configurations at $D = 0.02\lambda$.

higher total intensity leads to a higher SNR, or in a generalized Gaussian noise picture, where summing two independent Gaussian random variables (the x and y detector power flows) leads to a Gaussian random variable with a variance equal to the sum of the component variances. Since the x and y detector planes have roughly equal power flow and noise, both of these descriptions yield a factor of $\sqrt{2}$ difference in SNR between the individual and combined detector planes. As a result, a slightly lower SNR of 52.6 dB is used for the x and y detector planes ($10\log_{10}\sqrt{2} \approx 1.5$ dB). From the data shown in Fig. 6(a), it is clear that changes in separation smaller than $\lambda/1000$ can be distinguished with 2σ certainty. This certainty level of 2σ is commonly used for statistical confidence intervals, although others may instead be chosen, with corresponding effect on the minimum distinguishable change in separation.

The shapes of the curves in Fig. 6(a) are themselves interesting and provide insight into why resolutions far beyond the diffraction limit are available. If we consider the typical problem of distinguishing point sources or scatterers with direct imaging, we would find that, as the distance between the scatterers goes to zero, the CRB variance of an estimate of their separation will diverge to infinity. This is because, as the separation of point "sources" goes to zero, the derivative of the scattered field with respect to separation goes to zero. Since we measure the power flow from the fields, and the CRB variance is related to the reciprocal of this derivative, the CRB variance diverges. This behavior is well documented in the literature [31–35]. The divergence of the CRB as source separation goes to zero can be thought of as a fundamental reason for the diffraction limit. We do not see this divergence in Fig. 6(a) because the geometry of the scatterers prevents their center points from being brought closer together than their width, which effectively windows off the diverging part of the curves that we would see if we considered them as point objects. Additionally, the extra sensitivity provided by relative motion in structured illumination shifts the curves down, which abates the divergence of the CRB. Multiple scatter also provides additional sensitivity that moderates the CRB degradation with decreasing D/λ, however, this has a much weaker effect than relative motion in structured illumination. With reducing scatterer size combined with decreasing
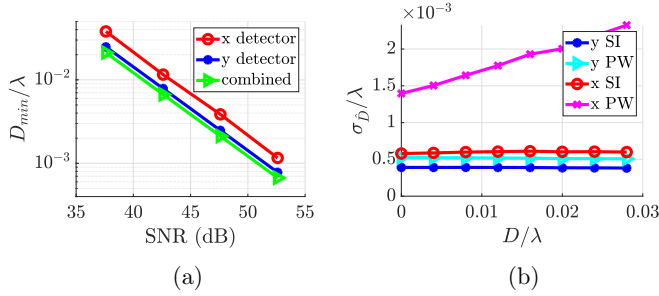
FIG. 7. Minimum scatterer separation distinguishable with 2σ certainty as a function of combined detector SNR, and comparison between Cramér-Rao bounds for estimating D with single-plane-wave illumination versus standing-wave illumination [structured illumination from (1)]. Both subfigures are scaled in terms of λ and use $\epsilon_r = 4$. (a) Minimum scatterer separation distinguishable from $D = 0$ with 2σ certainty as a function of SNR for three detector plane configurations with structured illumination. (b) Square root of the CRB variance of $\hat{D}$ as a function of D for plane-wave illumination (in each direction, and over the corresponding detector plane) and structured illumination (over each detector plane). 52.6-dB SNR. SI: structured illumination, PW: single-plane-wave illumination, y: y detector plane, x: x detector plane.

D, we would eventually see the CRB diverge, however, it does not in this case due to the indicated factors. Importantly, in relation to the point of this work, far-field data with relative motion in structured illumination provides additional sensitivity to D that moderates the divergence of the CRB.

Figure 6(b) shows the Fisher information, scaled by λ^2, over a phase scan of 2π, for each detector plane and the combined data. These curves provide additional insight into the difference in sensitivity between the two detector planes (x and y) and also demonstrate that measurements at field positions around $\Delta\phi_y = \pi$ provide little or no sensitivity to D. This occurs because $\Delta\phi_y = \pi$ corresponds to a null in the incident-field pattern at the center of the scatterers, and thus very little scattered power. The y detector plane provides greater Fisher information and thus higher resolution than the x detector plane, because the path-length difference between the scattering center of each particle is much larger when measured along the y detector plane than along the x detector plane. The resulting phase difference is one of the largest factors that causes the power flow through the detector to change with D, and thus the detector with more sensitivity to this phase difference provides greater resolution. Note that the Fisher information [$I(D)$] over $\Delta\phi_y$ is not directly comparable to the difference metric (g_s) over $\Delta\phi_y$, as the subtraction of reference values in (2) and (3) results in g_s containing data from multiple incident-field positions. While g_s provides a good metric for overall sensitivity, it does not explicitly relate to the sensitivity provided by each field position like the Fisher information. Of special note is that the x detector plane provides a standard resolution metric arrangement.

2. Other trends and illumination patterns

Consider now resolution as a function of the noise level. Figure 7(a) shows the minimum scatterer separation that can

be distinguished from $D = 0$ with 2σ certainty ($D_{\min}$) as a function of SNR. $D_{\min}$ is shown to decrease by about an order of magnitude for every 10-dB increase in the SNR, which is expected due to the constant CRB variance over the values of D considered. This trend is expected to continue for a SNR beyond the range shown, so for the situation leading to the results in Fig. 7(a), the diffraction limit cannot be exceeded if the SNR falls below about 30 dB. However, based on the analysis in Sec. II B and the bright-field nature of the measurement, 30 dB represents a relatively low SNR (that could easily be exceeded). Naturally, there is greater sensitivity shown in Fig. 7(a) to D with the y detector, because this directly exploits interference between the scattering centers of the two particles. Perhaps more relevant to applications is the far-subwavelength resolution with only the x detector, conforming to the usual arrangement for applications related to imaging.

The role of the structured illumination pattern in providing sensitivity to D is illustrated in Fig. 7(b). This figure shows $\sigma_{\hat{D}}$ for a measurement of the power flow through the x and y detector planes (right and top, respectively, in Fig. 2) as a function of D with a 52.6-dB SNR. Results are shown for the structured illumination pattern produced from the two interfering plane waves (Sec. II A) and for a single plane wave with $\mathbf{E} = [\exp(-jk_0y)]\hat{\mathbf{z}}$ for the y detector plane measurement or $\mathbf{E} = [\exp(-jk_0x)]\hat{\mathbf{z}}$ for the x detector plane measurement. The combined detector plane is not considered in this analysis because the single-plane-wave incident fields only produce significant power flow through one detector, and thus the data from the nonilluminated detector plane cannot be reasonably compared with the structured illumination results with the chosen (fixed-SNR) noise model. The plane-wave results shown in Fig. 7(b) are for 11 samples, matching the 11 samples taken at different values of $\Delta\phi_y$ in the structured illumination case. Using a single detector plane, the structured illumination cases each provide a smaller σ_D, and hence a higher spatial resolution, because the spatially varying incident field causes a measurable change in scatterer excitation when their separation is varied. The difference in resolution between the plane wave and structured illumination configurations depends on which detector plane is considered, as the y detector plane exploits interferometry between the particles while the x detector plane does not. It is clear from these results that measurement geometry has a significant effect on the degree to which far-subwavelength object information is encoded in a far-field measurement, and what factors enable that encoding.

The x detector, which is representative of a direct imaging arrangement, is the most relevant to optical microscopy. Notably, the Abbe diffraction limit is only applicable to this type of geometry, and not to the y detector measurements [26]. The x detector results are representative of a standard resolution metric (distinguishing laterally spaced point sources) which can be compared with prior literature. For this detector plane, sensitivity to far-subwavelength object features is provided primarily by relative motion in structured illumination. While there is still some sensitivity to D in the plane-wave case, the sensitivity falls off rapidly as D increases, indicating that this sensitivity is primarily provided by multiple scatter. As a result, if D is large, or if a less heavily scattering geom-

etry is considered, then the plane-wave case will be almost entirely insensitive to small changes in D, while the structured illumination case will retain its high sensitivity. We thus conclude, for typical optical measurements representative of microscopy, relative motion in structured illumination provides a very large increase in sensitivity.

For the y detector arrangement, which is sensitive to phase differences between scatter from each object, relative motion in structured illumination has a much smaller effect on sensitivity. This is because the geometry of the measurement in this case already provides very high sensitivity to D. This is perhaps unsurprising; the y detector geometry is more representative of an interferometer than a typical imaging problem, and thus far-subwavelength sensitivity should be expected with or without relative motion in structured illumination assuming sufficient SNR. With relative motion in structured illumination, the sensitivity of the x and y detectors is roughly equivalent. Relative motion in structured illumination can therefore be thought of as a means of accessing a level of sensitivity commensurate with an interferometric measurement in situations where the measurement geometry does not provide interferometric information.

While relative motion in a structured illumination pattern provides a significant improvement in sensitivity to D, as Fig. 7 indicates, it has another important role that should be addressed. With the single-plane-wave illumination pattern and a single-pixel detector, it is not possible to invert for more than one parameter of the object, as only one measurement can be performed. The structured illumination pattern allows for multiple measurements to be performed corresponding to different values of (ϕ_x, ϕ_y), which allows inversion for multiple parameters of the object, such as the two-parameter inversion for D and ϵ_r considered below in Sec. II F.

F. Inversion

The focus of this paper is on the far-subwavelength information available in the type of measurements we describe, and a variety of inversion techniques could be used in conjunction. As an example, we present here a method based on cost-function minimization to determine the subwavelength distance between scatterers and their relative permittivity. In this approach, f_n represents the noisy data that would be obtained from an experiment, and f represents the noiseless data calculated from the forward model. To show that these approaches can yield sensitivity to a difference of 0.01λ in separation and a difference of 0.5 in relative permittivity at 54.1-dB SNR, we minimize a cost function

$$(D^*, \epsilon_r^*) = \arg \min_{D, \epsilon_r} \sum_{\Delta x, \Delta y} |f_{n,\text{motion}}(\Delta x, \Delta y; D, \epsilon_r)$$
$$- f_{\text{motion}}(\Delta x, \Delta y; D, \epsilon_r)|, \quad (7)$$

for the case of object motion in structured illumination. This cost function uses the function f described in (2), as opposed to the function g plotted in Sec. II D; this is because f contains sufficient information for inversion, while g is merely a visualization tool (see Sec. II C). Noisy data corresponding to all values of $D \in [0, 0.05\lambda]$ and $\epsilon_r \in [11.9, 14.4]$ are compared with noiseless data for $(D, \epsilon_r) = (0.02\lambda, 12.4)$. We find that
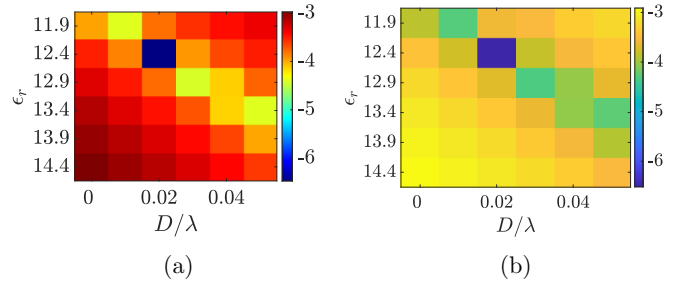

FIG. 8. Logarithm of mean value of the cost function comparing noisy data for $D = 0.02\lambda$ and $\epsilon_r = 12.4$ and noiseless data for (a) object translation and (b) phase scanning of the structured field. Cost function minimum is obtained at the correct value of separation and dielectric constant within a margin of $\lambda/100$ for separation and 0.5 for dielectric constant.

the cost is minimum for $(D^*, \epsilon_r^*) = (0.02\lambda, 12.4)$, as is shown in Fig. 8(a). Referring to Fig. 2, the object is moved in steps of 0.1λ over a square region of side 5λ. The separation (D) is varied in steps of 0.01λ, from 0λ to 0.05λ. The relative permittivity of the object, ϵ_r, is varied in steps of 0.5, from 11.9 to 14.4. For every value of $(\Delta x, \Delta y; D)$, the noisy data are compared with the noiseless data of a chosen value of $(D, \epsilon_r) = (0.02\lambda, 12.4)$. The logarithm of the mean cost obtained from the 100 sets of noisy data is shown in Fig. 8(a). It is evident that the lowest cost is obtained for the correct value of $(D, \epsilon_r) = (0.02\lambda, 12.4)$.

When the background field is scanned over the object, rather than the object moving in the field, as in (7), the phase $\Delta \phi_x$ of one of the incident waves is varied from 0 to π in steps of 0.2π while $\phi_y = 0$. The separation D is varied in steps of 0.01λ from 0λ to 0.05λ and the relative permittivity ϵ_r is varied identically as before. For every value of ϕ_x between 0 and π, noisy data are compared with the noiseless data for $(D, \epsilon_r) = (0.02\lambda, 12.4)$. We minimized a cost function as

$$(D^*, \epsilon_r^*) = \arg \min_{D, \epsilon_r} \sum_{\Delta \phi_x} |f_{n,\text{scan}}(\Delta \phi_x; D, \epsilon_r)$$
$$- f_{\text{scan}}(\Delta \phi_x; D, \epsilon_r)|. \quad (8)$$

The logarithm of the mean cost obtained from 100 noisy datasets is shown in Fig. 8(b). It is evident that the minimum cost is obtained at the correct value of $(D, \epsilon_r) = (0.02\lambda, 12.4)$.

The cost function plots in Fig. 8 show that both motion in structured illumination and scanning of structured illumination can yield information in the far-field scattered field intensity that is sensitive to a change of 0.01λ in scatterer separation and a change of 0.5 in relative permittivity of the scatterers, despite the presence of significant detector noise. This is the case even when D and ϵ_r are being simultaneously estimated, rather than the one-parameter inversion analyzed in Sec. II E.

III. SPECKLE ILLUMINATION

In many applications, coherent light from a laser forms speckle because of the random scatter involved when the light interacts with surface or bulk scattering features, and various
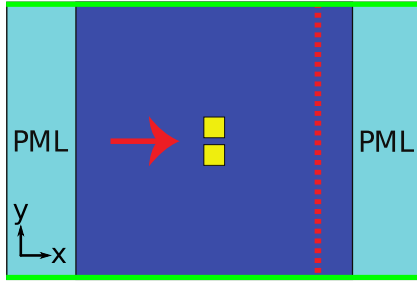
FIG. 9. Adaptation of the geometry shown in Fig. 2 for use with a speckle field, which is incident from the left. The left and right boundaries are still 2λ-thick PMLs, but the top and bottom boundaries (green) have been replaced with continuous periodic boundary conditions.

FIG. 10. Speckle results, with $\epsilon_r = 4$ and 100 samples at 40-dB SNR. (a) 1 speckle field. (b) Average over 20 speckle fields.

fundamental and applied aspects of statistical optics have received substantial recent attention. For instance, a means to access the transmission matrix and hence focus through scattering media has been found [36]. Also, speckle correlations over frequency provide information about the random medium [37,38], and correlations over object position offer a way to image an object in a heavily scattering random background [39,40]. More generally, interesting transport physics has been found with coherent fields in randomly scattering media, including the role of participating modes on the eigenvalue distribution [41] and in relation to localization [42] and quantum transport [43,44]. We show that speckle can provide the structured illumination that allows for superresolution sensitivity and inversion with relative motion between this field and the object. As in Sec. II, this is investigated using a stationary object and translating the field.

A. Speckle setup

The notation for this section is similar to that of Sec. II, where appropriate, but the differing incident field necessitates some changes. The function $g(p_x, p_y; D)$, defined in (3), represents the difference between a noisy single-pixel measurement and a noise-free reference value, which is generated using the forward model. To address the speckle case, we define $g_s(\Delta\phi_x, \Delta\phi_y; D)$. This g_p corresponds to the motion of a speckle field (which will only be moved in the y direction), and this spatial translation is described by the variable $\Delta\gamma_y$ [and not Δy, which is used in Sec. II in relation to object motion using $g_s(\Delta\phi_x, \Delta\phi_y; D)$]. A fixed-SNR Gaussian noise model equivalent to the model presented in Sect. II B is also used for the speckle results. A slightly lower SNR of 40 dB is used to illustrate good performance at this SNR.

In the numerical FEM simulations with speckle, we consider the geometry shown in Fig. 9, which is transversely periodic and hence has a discrete plane-wave expansion. Only a single detector geometry is considered in order to clearly isolate the effect of the speckle illumination pattern from other factors. The detectors on the right measure the intensity, but these data are only used to calculate the total power flow. Noise is then added to this single-pixel detector data. A speckle field is generated that illuminates the sample from the left side, propagating in the positive x direction and spanning the full breadth of the y dimension. Let the size of the domain
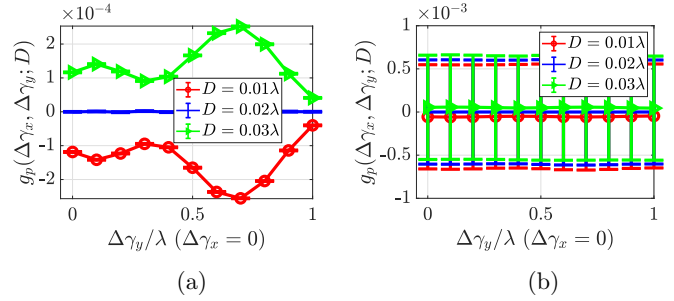
in the y direction be L_y. In order for the speckle field to be periodic in the y dimension, the y components of the wave numbers of its plane-wave components k_y must each be integer multiples of L_y, i.e., $k_y(m) = 2\pi m/L_y$, for some integers m. Also, in order to ensure that there are no evanescent field components in this speckle field, we must limit m such that $k_x(m) = [k_0^2 - k_y(m)^2]^{1/2}$ is real, or $|m| \leqslant L_y/\lambda$. The speckle field is composed of a superposition of such plane waves.

The complex amplitudes of these plane waves are drawn from a random distribution, resulting in random speckle. The real and imaginary components should be independent and identically distributed zero-mean Gaussian random variables [45]. Therefore, if the maximum allowable value of m (as described in the preceding paragraph) is $M = \lfloor L_y/\lambda \rfloor$, then $2M + 1$ random complex amplitudes should be generated (including the $m = 0$ mode), or $2(2M + 1)$ independent samples drawn from a zero-mean Gaussian distribution. Let these amplitudes be denoted α_m. This process is repeated for each random speckle field that is generated. The speckle field can therefore be written as

$$\mathbf{E}_p = \left\{ \sum_{m=-M}^{M} \alpha_m e^{(-jxk_x(m) - j(y+\Delta\gamma_y)k_y(m))} \right\} \hat{\mathbf{z}}. \quad (9)$$

Comparing (9) to (1), $\Delta\gamma_y$ has units of distance, whereas ϕ_x and ϕ_y have units of phase. The translation in (9) along the y direction is accomplished by the phase ramp with slope $\Delta\gamma_y$.

B. Speckle illumination results

Figure 10 shows the speckle results. The speckle field is translated across a stationary object; in this case, referring to (3), the parameter p_y corresponds to the distance by which the speckle is shifted, $\Delta\gamma_y$, while p_x goes unused because the field is not shifted in the x direction. When a single random speckle field is used, Fig. 10(a) shows distinguishability among different separations D, demonstrating that the far-subwavelength resolution obtained with this method does not rely solely on the type of field described in Sec. II. The shape of the curves differs from those in Sec. II D due to the relative irregularity of the speckle field compared with the standing wave, although this has not detracted from distinguishability. The inversion approach described by (8) assumes the ability to construct a forward model, and this requires knowledge of the speckle field that is used. This information would be difficult to obtain if the speckle field were generated by passing coherent light through a scattering medium. However, using a spatial light
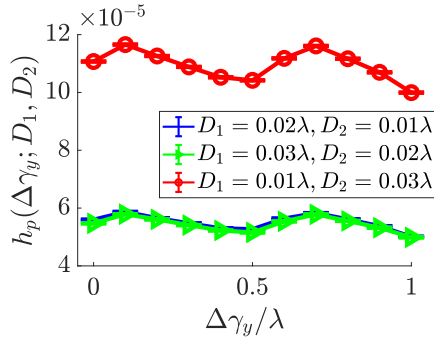
FIG. 11. Mean absolute difference $h_p(\Delta\gamma_y; D_1, D_2)$ for two different values of D, averaged over 20 random speckle fields. This allows many random fields to be averaged over without resulting in the significant overlap shown in Fig. 10(b) and demonstrates distinguishability (but not reconstruction) of D.

modulator (SLM) would allow such a forward model to be constructed and D to be estimated.

If the speckle pattern is not known, then inversion for D becomes more challenging. Figure 10(b) shows the result for g_p with averaging over 20 random speckle fields. While the curves from a single speckle field are distinguishable, the averaged curves are not for the three separation values. This is because there is no consistent relationship between $g_p(\Delta\gamma_y; D)$ and the separation D when different speckle fields are used. The different intensity patterns produced by each of the speckle fields causes g_p to behave differently as a function of D and $\Delta\gamma_y$ for each speckle field, and over a large number of speckle fields, g_p averages out to approximately zero. As a result, g_p cannot reliably be used to invert for D if the speckle pattern is unknown.

Model-free far-subwavelength resolution

A distinction between two goals must be recalled: establishing sensitivity to far-subwavelength changes in D, and using this sensitivity to estimate the separation D. While the above discussion of the relationship between Figs. 10(a) and 10(b) involves limitations on inversion, it does not comment on the basic question of sensitivity. This section shows that, if the goal is to distinguish between two values of D, then some benefit could still be gained from using multiple speckle fields. To distinguish between $D = D_1$ and $D = D_2$, the mean absolute difference

$$h_p(\Delta\gamma_y; D_1, D_2) = \langle|f_n(\Delta\gamma_y; D_1) - f_n(\Delta\gamma_y; D_2)|\rangle \quad (10)$$

can be calculated, where the brackets $\langle\cdot\rangle$ indicate averaging over the random speckle fields, and f_n again represents a noisy measurement of power flow across the entire detector plane. This metric is adapted from (7), where the mean absolute difference is used to compare a noisy measurement to a noiseless simulation. Here, it instead compares two noisy measurements. The calculated result using (10) is plotted in Fig. 11 using the same 20 speckle fields as in Fig. 10(b).

The distinguishability in Fig. 11 is accomplished without using the forward model $f(p_x, p_y; D)$, meaning that the far-subwavelength changes in D can be sensed without prior knowledge of either the background field or the geometry.

This is a core result of the paper because it shows that this far-subwavelength sensitivity results from relative motion with structured illumination, not merely from prior knowledge.

Because Fig. 11 shows the mean absolute distance between noisy measurements, rather than the measurements themselves, an overlap between two curves does not indicate a lack of distinguishability. Rather, the distance from zero of each curve indicates the ability to discern between a separate pair of values of D. A tentative pattern is suggested that, when the difference between D_1 and D_2 is doubled, the mean absolute difference is also doubled, although more work is required to fully establish this pattern. The overlap of the blue and green curves in Fig. 11 shows that g_p changes about the same amount when D is increased from 0.01λ to 0.02λ as it did when increasing from 0.02λ to 0.03λ. This explains why the red curve in Fig. 11 is about twice either the green or blue curve, as well as why the curves in Figs. 3–5 and 10 are symmetric about $D = 0.02\lambda$. More generally, (10) can be thought of as measuring the possible level of sensitivity achievable if a forward model is available for the incident field, as is assumed in (7) and (8). However, if these g_p are not averaged together, then a more elaborate cost-function-based inversion method could be used. In this case, taking into account the g_p due to each random speckle field may improve inversion performance, as Fig. 11 shows that many such speckle fields contain information that can be used for distinguishing different values of D. While the effect of the speckle correlation length (speckle size) or contrast ratio is not explored, it is reasonable to assume that optimal performance occurs with small speckle (of size $\lambda/2$) that is fully developed (speckle contrast ratio of 1).

IV. DISCUSSION

We have shown that either a moving background field with a stationary object or object motion in a structured field can yield far-subwavelength spatial resolution information appropriate for imaging. Despite the loss of evanescent fields and thus of high-spatial-frequency information in the far field, information about nanoscale features is still available in the propagating plane-wave spectrum. This is because such nanoscale changes in object geometry have a small effect on the propagating spectrum, which is greatly enhanced by relative motion in structured illumination. With the use of a sufficiently constrained forward model, the approach presented is equivalent to estimating the high-frequency components of the plane-wave spectrum from measurements of its low-frequency components, modulated by motion in the structured field. While it is well known that modifying a structure changes the complete plane-wave spectrum, the degree to which far-subwavelength information can be extracted from the propagating spectrum and the role of relative motion in structured illumination in enhancing sensitivity to this information was not well understood until now. We should note that this is different from an interferometer, where counter-propagating waves provide interference fringes that are very sensitive to mirror placement [26]. While interferometry can also provide sensitivity to nanoscale features from an optical measurement, as demonstrated in Sec. II E, our approach provides access to nanometer-scale object information even

with measurement geometries that are not sensitive to phase differences across the object. Additionally, our approach allows unique inversion for multiple features from a single measurement, further distinguishing it from traditional interferometry. Our work has shown that, using the standard imaging arrangement, hence the x detector plane in Fig. 2(a), available equipment will allow a spatial resolution of about one-thousandth of a wavelength.

It was previously shown that the level of granularity accessible in material is related to the plane-wave spectrum extent, relevant for homogenization in an imaging system [46]. Now we know that essentially unlimited and fine granularity in condensed matter is accessible with relative motion in a structured field. We have also demonstrated that the achieved spatial resolution is not limited to an illumination pattern composed of two interfering plane waves but can be obtained using a speckle pattern as well. This further implies that a wide variety of illumination patterns could potentially be used, so long as the spatial variation of the pattern is sufficiently high. Finally, we have shown that, while prior knowledge of the incident field and geometry allow the reconstruction of nanometer-scale features, changes on this scale can be detected even without such knowledge.

Analysis using information theory provides insight into the role of key factors including the illumination pattern, a constrained forward model, and the object geometry in achieving far-subwavelength resolution. While all three are important to resolution, structured illumination can be considered more critical than the forward model in the situations considered: relaxing the one-parameter inversion to two-parameter still results in high resolution (Sec. II F), but using single-plane-wave illumination reduces resolution and does not allow multiparameter inversion. Furthermore, the fact that $\sigma_{\hat{D}}$ does not have a limiting asymptote as $D \to 0$ in Fig. 6(b) implies that the resolution at which D can be estimated can be increased arbitrarily by increasing the SNR. These insights are likely also applicable to the measurement problems explored in earlier work [24,25]. While it is not explicitly considered in our analysis, utilizing a multipixel detector or a spatially distributed detector network with relative motion in structured illumination would provide additional information, enabling inversion for additional far-subwavelength object features.

This work has provided the physical basis for superresolution sensing with relative motion in structured illumination and an assessment of the expected possible resolution. The results also break several key requirements that were previously assumed necessary for far-subwavelength sensing and inversion using relative motion in structured illumination [24], notably the need for object motion in a known structured illumination pattern. Motion of the fields, rather than the object, allows for measurements that are both faster and more robust, and the extension to arbitrary illumination patterns provides significant additional flexibility in the experimental implementation. Being able to access such high spatial resolution without a forward model (with a known incident field in a cost function involving measurements) also opens substantial new application domains, such as for photonics in biophysical studies, including of the brain. The unprecedented resolution available with this approach presents a variety of important application domains, such as unlabeled protein

sensing and material defect detection. Because this work motivates an experimental study, we have proposed a possible implementation in Appendix C.

While unique inversion for nanoscale object features with our approach requires prior information in the form of a forward model, there are many applications for which this information would be readily accessible. For example, constraints on the object may be available during material inspection, where subwavelength defects must be detected, or in protein imaging, where the typical structure of a protein can be known. While the simulated object in this paper has been of subwavelength size, this is a choice made for computational simplicity, and the results shown here should extend naturally to far-subwavelength features of larger objects as well. Objects that interact more strongly with each other provide more information as well; this has been exploited by, for example, tomographic diffraction microscopy [47,48], which can also utilize inversion constraints on the dielectric constant of the object based on prior knowledge of the sample in order to improve resolution (as has been used in Sec. II E).

This line of work can be understood as a special case of single-pixel imaging [15,16] (SPI), and it reveals the framework's power to extract far-subwavelength features when combined with a suitable forward model. Some approaches make only a random subset of measurements and use compressive-sensing-based reconstruction techniques [16], and some use light sources that produce correlated photon pairs [49]. While these approaches typically attempt to accommodate a general class of images, the forward model employed here incorporates specifics from the imaging target, similar to how the camera itself is modeled in image-processing-based superresolution reconstruction methods [50]. Compressive sensing generally involves assuming that the image is sparse under a particular basis or other set of functions [51–53], and the forward model used in this paper can be considered a further degree of prior knowledge. This work demonstrates that the resolving power of such structured illumination methods can be greatly improved if a forward model is specifically tailored to the object being imaged, or if relative motion is introduced. Some SPI methods modulate the light at the detector instead of the illumination and are correspondingly referred to as "structured detection" rather than "structured illumination" [15]. The placement of a scattering analyzer between the object and detector [54] can be considered a form of structured detection that enables subwavelength far-field sensitivity by leveraging relative motion with structured illumination [55], but the randomness of the scattering medium may be difficult to precisely characterize with a nonrandom forward model of the type used in this paper.

Outside of SPI, phase-translated standing-wave patterns have been used for increased axial resolution [56] (standing-wave fluorescence microscopy) and sub-Rayleigh lateral resolution [1] (structured illumination microscopy, or SIM). SIM has been adapted for the use of random speckle illumination [3,57], with image reconstruction being done using either cost-function inversion [3] or second-order image statistics [57], or with single-pixel detection and spatiotemporally modulated illumination [58]. All of these methods exploit structured illumination for improved resolution but are limited

by the number of unknowns involved in reconstructing arbitrary images. Our results suggest that the resolution of some of these methods may be improved with the inclusion of a highly constrained forward model and relative motion between the sample and the illumination.

While our results with random speckle illumination only show sensitivity to far-subwavelength features, rather than full invertibility, unique inversion for object features may be possible in this case with an appropriate measurement strategy and forward model. As noted in the previous paragraph, second-order image statistics have been used to replicate the resolution benefit of SIM using random speckle illumination [57] without relative motion. Additionally, speckle intensity correlations over object position have been demonstrated as a basis for extracting object information from a speckle image without knowledge of the underlying speckle pattern [59]. Either of these strategies could likely be combined with our approach to invert for far-subwavelength object features. This would still require a highly constrained model for object geometry but would allow inversion with random speckle illumination. Both of these approaches to inversion would probably necessitate measurements using a multipixel detector or camera, as opposed to the single-pixel detector used in this paper. Inverting for features using image statistics would additionally require collecting data over a sufficient statistical sample of random illumination patterns, which could be achieved by translating the object over many speckle correlation lengths.

The results presented in this paper consider the case of perfectly coherent illumination and scatter; however, they could likely be extended to situations with limited coherence, although with reduced sensitivity. By way of example, a similar information-theory analysis to Sec. II E has been performed for a measurement of the separation of two fluorophores [60] and indicated a maximum resolution of around 10 nm ($\approx \lambda/50$) without structured illumination. In this case, subdiffraction-limit resolution is achieved due to the highly constrained single-parameter estimation. In the x-ray regime, it has been demonstrated that the positions of a set of scatterers can be imaged with comparable or improved resolution compared with coherent approaches using incoherent measurements of intensity correlations over wave-vector [61]. As a result, far-subwavelength resolution based on relative motion may still be achievable even if coherence requirements are relaxed significantly. The problem of distinguishing incoherent point sources with various approaches has received substantial attention [6,7,31–35], and it has been shown that partial coherence results in a looser bound on resolution [62]. Partially coherent structured illumination may arise, for example, when broadband light is passed through an optical bandpass filter. For speckle illumination, reducing the coherence also reduces the speckle contrast ratio [45], and exploration may be done into the relationship between the speckle contrast ratio and the sensitivity using relative motion in a speckle field. Prior studies on the statistical properties of broadband speckle [63] would be useful in such an effort.

V. CONCLUSION

We have shown that relative motion between structured illumination and an object provides sensitivity to far-subwavelength object features using far-field measurements, despite the presence of realistic detector noise. There are three primary contributions in this work. (i) Intensity measurements in the far field with either structured field scanning over an object or motion of the object in a stationary structured field provide access to virtually unlimited lateral spatial resolution. (ii) Our understanding is that superresolution sensitivity exists with relative motion because motion in a structured field greatly enhances changes to the propagating spectrum induced by the nanostructure, and information theory supports this position. (iii) Far-subwavelength information is available with a known forward model, and, importantly, even when the specific incident fields are unknown. If suitable constraints on the geometry are available, then inversion for parameters of the object is possible and an image could thus be formed. The advantage of using the field-scanning approach is that it can be faster and more robust than spatial scanning (which needs a nanometer-precision mechanical stage with good repeatability), potentially important in some applications. Instead of structured light from two plane waves incident on the object, a spatial light modulator would allow a complex set of incident fields to be realized and scanned over the object, such as the demonstrated speckle field. Adequate temporal coherence for the laser light is required, and, while maintaining low noise is important, there are inexpensive lasers that fulfill this requirement. The performance could be enhanced with multiple-detector data, so that higher spatial resolution becomes available.

APPENDIX A: NUMERICAL ACCURACY

This Appendix describes details of the simulation related to numerical accuracy. The accuracy of an FEM simulation depends on the size of the mesh elements, and this is therefore a critical parameter. For plane-wave illumination, it is determined that satisfactory accuracy is achieved using a mesh composed of triangular elements with a maximum side length of 0.02λ and a minimum size of 0.001λ. At this level of discretization, there are at least eight layers of mesh elements between the two scatterers at every value of D. These values are also judged to provide sufficient accuracy in Ref. [24]. The process by which these mesh sizes are decided upon is the same for the plane-wave-illumination case as for the speckle-illumination case, and it is presented in more detail for the latter.

For speckle illumination, the maximum element size is $\lambda/20$ in the PML (where less sensitivity to the mesh element size is found), $\lambda/40$ in the background, and $\lambda/(40n)$ in the dielectric material (where n is the refractive index of this material). Values between the mesh element points are interpolated using a cubic interpolation method, instead of the quadratic method used for plane-wave illumination, allowing
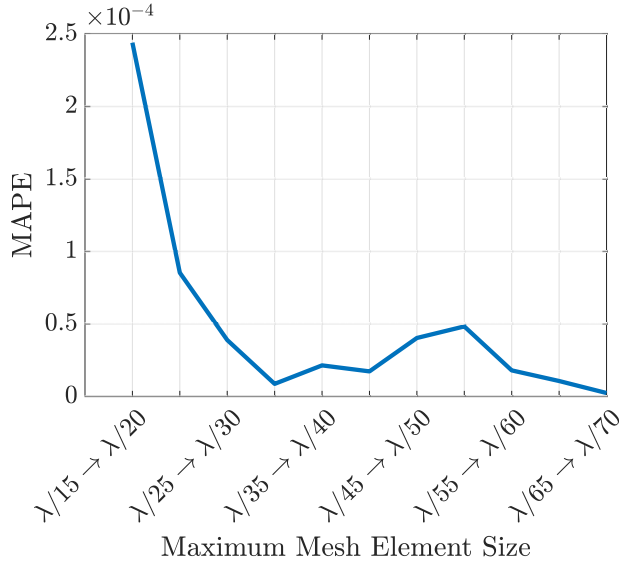
FIG. 12. Mean absolute percent error (MAPE) in $g_p(\Delta\gamma_y; D)$ when decreasing the maximum mesh element size, calculated for one speckle field [the same one used in Fig. 10(a)]. Parameter values of $D = 0.01\lambda$ and $\epsilon_r = 4$ are used. Any decrease in the maximum mesh element size beyond $\lambda/25$ results in a MAPE less than 0.0001%, so our chosen maximum size of $\lambda/40$ is clearly sufficient for numerical convergence.

a coarser mesh. The minimum element sizes are smaller than the maxima by a factor of 10, with an additional factor of 10 near narrow regions.

To verify the numerical accuracy of our results, the maximum FEM element size is varied until convergence in the results is achieved, and the results of this process are shown in Fig. 12. The first speckle field [the same one used in Fig. 10(a)] is repeatedly applied to the geometry, while the maximum element size (for the background, and dielectric correspondingly) is iteratively reduced. The change between successive resulting $g_p(\Delta\gamma_y; D)$ curves is compared using an absolute percentage error metric, with parameter values of $D = 0.01\lambda$ and $\epsilon_r = 4$. This is calculated at each value of $\Delta\gamma_y$, and then averaged together, yielding a mean absolute percentage error (MAPE) as

$$\mathrm{MAPE}\left(\frac{\lambda}{d_a} \to \frac{\lambda}{d_b}\right) = \frac{100\%}{N}$$
$$\times \sum_{i=1}^{N} \left| \frac{G_i\left(\frac{\lambda}{d_b}\right) - G_i\left(\frac{\lambda}{d_a}\right)}{G_i\left(\frac{\lambda}{d_a}\right)} \right|, \quad (A1)$$

where N is the number of different values of $\Delta\gamma_y$ calculated ($N = 11$, in this case), and $G_i(\lambda/d) = g_p(\Delta\gamma_y; D)$ for the ith value of $\Delta\gamma_y$ and a maximum mesh element size of λ/d.

As shown in Fig. 12, decreasing the maximum mesh element size of the background from $\lambda/20$ to $\lambda/25$ [and of the dielectric to $\lambda/(25n)$, accordingly] results in a mean absolute change in $g_p(\Delta\gamma_y; D)$ of less than 0.0001%, as did any further decrease. We therefore expect no issues of numerical accuracy with our chosen maximum element size of $\lambda/40$ [and $\lambda/(40n)$ for the dielectric].
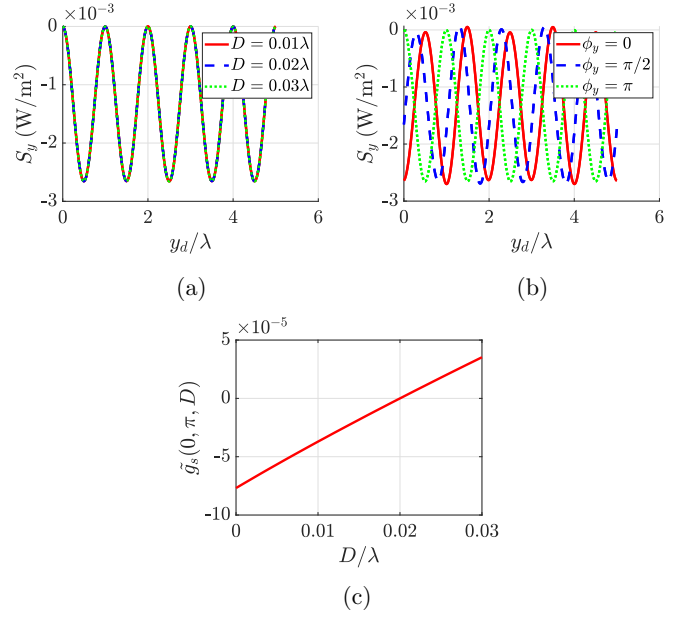

FIG. 13. Detailed information about the measurements underlying Sec. II. (a) Poynting vector incident upon the y detector at different positions, for varying D. The change in intensity is small compared with the background. y_d/λ represents the position on the y detector plane normalized in terms of wavelength. (b) Similar, but for a changing field position instead. The measurement is laterally translated. (c) Measured power difference for a fixed field position, but more separation values D, and having been divided by the background intensity according to (B1). This illustrates required detector sensitivity.

APPENDIX B: NORMALIZED SENSITIVITY

For plane-wave illumination, the intensity incident upon the system was on the order 10^{-3} W/m, using units corresponding to the 2D geometry. Equivalently, this intensity could be described as 10^{-3} W/m^2 if a three-dimensional (3D) geometry is considered where none of the quantities vary in one spatial dimension. Such will be the convention used here, for familiarity with units of 3D space. This intensity is approximately equal to that incident upon the detector plane, because the object has a small scattering cross section. The change in intensity depends on the setup, but is typically on the order 10^{-7} W/m^2, as measured by averaging over intensity-detector points in (2). Normalizing this intensity change with respect to the intensity incident upon the system gives a factor of 10^{-4}; to detect the specified changes in D, a detector sensitivity to changes of 1 part in 10,000 is necessary. For the speckle illumination, the intensity incident upon the system is on the order of 10^{-1} W/m^2, but the sensitivity requirement is similar. This sensitivity requirement corresponds to a SNR of 40 dB. Using modern avalanche photodiodes [64], this SNR is achievable [24]. An experimental evaluation of one CCD camera found a SNR of about 30 dB per pixel [65], and averaging over its 400 pixels increases this SNR to over 40 dB. Section II B discusses this issue further.

Figures 13(a) and 13(b) show plots of the Poynting vector over the top detector plane (y detector) for the plane-wave illumination case of Sec. II [described

by (1)] at various values of D [Fig. 13(a)] and ϕ_y [Fig. 13(b)], with $\phi_x = 0$ and $\epsilon_r = 4$. Figure 13(c) shows an example normalized version of the difference signal g_s as a function of D. The normalized difference is given by

$$\tilde{g}_s(\phi_x, \phi_y, D) = \frac{g_s(\phi_x, \phi_y, D)}{\int \mathbf{S}(x, y; \phi_x, \phi_y, D) \cdot \hat{\mathbf{n}} ds} \quad \text{(B1)}$$

and represents the ratio of the difference signal to the total power flow through the detector plane.

APPENDIX C: CONSIDERATIONS FOR EXPERIMENTAL ADAPTATION

An experimental realization of this work would be relatively straightforward to implement and a general framework for a possible experimental adaptation is presented in Fig. 14. The scales and distances used in the simulations were chosen with computational constraints in mind, but they are too small to realistically implement in an experiment. To account for this, a system of lenses should provide comparable performance. Figure 6 demonstrates that only one detector orientation is necessary to access far-subwavelength sensitivity, so a more complicated experimental arrangement with two perpendicular detector planes (as in Fig. 2) would not be needed. Our results also demonstrate that nanoscale information is accessible with a wide variety of illumination patterns, allowing for one to be chosen based on the desired geometry of the experiment, potentially further simplifying the required setup. Experimental realization of this approach could enable applications in material defect detection and protein imaging (where contrast might be provided with a fluorophore, if the coherence requirements can be met using a bandpass filter).
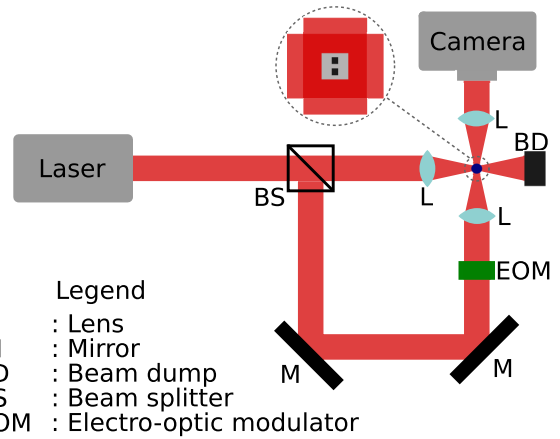

FIG. 14. Conceptual diagram for a possible experimental adaptation. A laser is focused onto a structured sample, and an electro-optic modulator translates the field along one direction by modulating its phase.

The potential noise due to errors in mechanical positioning and electronic phase control in corresponding experimental realizations of these concepts has not been incorporated. The results from beam motion in Fig. 3, and object motion in Fig. 4, have relatively similar features. We attribute differences to the specific object geometry and scan ranges in relation to the detection arrangement. For the geometry considered, a larger dielectric constant provides greater sensitivity, as of course does higher SNR (from longer integration time or reduced detector noise). Technically, beam scanning could be achieved with high speed. This makes the phase-scanning approach or, more generally, electronic control of the incident field as a means of relative motion with respect to the object, of substantial practical utility.

[1] M. G. Gustafsson, Surpassing the lateral resolution limit by a factor of two using structured illumination microscopy, J. Microsc. **198**, 82 (2000).

[2] R. Heintzmann and C. G. Cremer, Laterally modulated excitation microscopy: Improvement of resolution by using a diffraction grating, Proc. SPIE **3568**, 185 (1999).

[3] E. Mudry, K. Belkebir, J. Girard, J. Savatier, E. Le Moal, C. Nicoletti, M. Allain, and A. Sentenac, Structured illumination microscopy using unknown speckle patterns, Nat. Photonics **6**, 312 (2012).

[4] G. H. Yuan and N. I. Zheludev, Detecting nanometric displacements with optical ruler metrology, Science **364**, 771 (2019).

[5] K. Edamatsu, R. Shimizu, and T. Itoh, Measurement of the photonic de Broglie wavelength of entangled photon pairs generated by spontaneous parametric down-conversion, Phys. Rev. Lett. **89**, 213601 (2002).

[6] S. Oppel, T. Büttner, P. Kok, and J. von Zanthier, Superresolving multiphoton interferences with independent light sources, Phys. Rev. Lett. **109**, 233603 (2012).

[7] A. Classen, F. Waldmann, S. Giebel, R. Schneider, D. Bhatti, T. Mehringer, and J. von Zanthier, Superresolving imaging of arbitrary one-dimensional arrays of thermal light sources using multiphoton interference, Phys. Rev. Lett. **117**, 253601 (2016).

[8] O. Schwartz and D. Oron, Improved resolution in fluorescence microscopy using quantum correlations, Phys. Rev. A **85**, 033812 (2012).

[9] D. Gatto Monticone, K. Katamadze, P. Traina, E. Moreva, J. Forneris, I. Ruo-Berchera, P. Olivero, I. P. Degiovanni, G. Brida, and M. Genovese, Beating the Abbe diffraction limit in confocal microscopy via nonclassical photon statistics, Phys. Rev. Lett. **113**, 143602 (2014).

[10] A. Classen, J. von Zanthier, M. O. Scully, and G. S. Agarwal, Superresolution via structured illumination quantum correlation microscopy, Optica **4**, 580 (2017).

[11] K. M. Berland, P. T. So, Y. Chen, W. W. Mantulin, and E. Gratton, Scanning two-photon fluctuation correlation spectroscopy: Particle counting measurements for detection of molecular aggregation, Biophys. J. **71**, 410 (1996).

[12] S. W. Hell and J. Wichmann, Breaking the diffraction resolution limit by stimulated emission: Stimulated-emission-depletion fluorescence microscopy, Opt. Lett. **19**, 780 (1994).

[13] M. J. Rust, M. Bates, and X. Zhuang, Sub-diffraction-limit imaging by stochastic optical reconstruction microscopy (STORM), Nat. Methods **3**, 793 (2006).

[14] E. Betzig, G. Patterson, R. Sougrat, O. Lindwasser, S. Olenych, J. Bonifacino, M. Davidson, J. Lippincott-Schwartz, and H.

Hess, Imaging intracellular fluorescent proteins at nanometer resolution, Science **313**, 1642 (2006).

[15] G. M. Gibson, S. D. Johnson, and M. J. Padgett, Single-pixel imaging 12 years on: A review, Opt. Express **28**, 28190 (2020).

[16] M. F. Duarte, M. A. Davenport, D. Takhar, J. N. Laska, T. Sun, K. F. Kelly, and R. G. Baraniuk, Single-pixel imaging via compressive sampling, IEEE Signal Process. Mag. **25**, 83 (2008).

[17] C. F. Higham, R. Murray-Smith, M. J. Padgett, and M. P. Edgar, Deep learning for real-time single-pixel video, Sci. Rep. **8**, 2369 (2018).

[18] A. Sakdinawat and D. Attwood, Nanoscale x-ray imaging, Nat. Photonics **4**, 840 (2010).

[19] F. Pfeiffer, X-ray ptychography, Nat. Photonics **12**, 9 (2018).

[20] J. M. Rodenburg and H. M. Faulkner, A phase retrieval algorithm for shifting illumination, Appl. Phys. Lett. **85**, 4795 (2004).

[21] M. Dierolf, P. Thibault, A. Menzel, C. M. Kewish, K. Jefimovs, I. Schlichting, K. von Koenig, O. Bunk, and F. Pfeiffer, Ptychographic coherent diffractive imaging of weakly scattering specimens, New J. Phys. **12**, 035017 (2010).

[22] S. C. Park, M. K. Park, and M. G. Kang, Super-resolution image reconstruction: A technical overview, IEEE Signal Process. Mag. **20**, 21 (2003).

[23] A. M. Maiden, M. J. Humphry, F. Zhang, and J. M. Rodenburg, Superresolution imaging via ptychography, J. Opt. Soc. Am. A **28**, 604 (2011).

[24] K. J. Webb, Y. Chen, and T. A. Smith, Object motion with structured optical illumination as a basis for far-subwavelength resolution, Phys. Rev. Appl. **6**, 024020 (2016).

[25] D. Lin, V. Raghuram, and K. J. Webb, Determining optical material parameters with motion in structured illumination, Opt. Express **30**, 46010 (2022).

[26] M. Born and E. Wolf, *Principles of Optics*, 7th Expanded Edition (Cambridge University Press, Cambridge, 2005).

[27] COMSOL AB, Stockholm, Sweden, Comsol multiphysics® v. 6.1 (2021), http://www.comsol.com/.

[28] N. G. van Kampen, *Stochastic Processes in Physics and Chemistry*, 3rd ed. (Elsevier, Amsterdam, 2007).

[29] D. Middleton and Institute of Electrical and Electronics Engineers, *An Introduction to Statistical Communication Theory* (McGraw-Hill, New York, 1960).

[30] S. M. Kay, *Fundamentals of Statistical Signal Processing*, Prentice Hall Signal Processing Series (Prentice-Hall PTR, Englewood Cliffs, 1993).

[31] M. Tsang, Resolving starlight: A quantum perspective, Contemp. Phys. **60**, 279 (2019).

[32] W.-K. Tham, H. Ferretti, and A. M. Steinberg, Beating Rayleigh's curse by imaging using phase information, Phys. Rev. Lett. **118**, 070801 (2017).

[33] S. Zhou and L. Jiang, Modern description of Rayleigh's criterion, Phys. Rev. A **99**, 013808 (2019).

[34] M. Tsang, R. Nair, and X.-M. Lu, Quantum theory of superresolution for two incoherent point sources, Phys. Rev. X **6**, 031033 (2016).

[35] Z. Yu and S. Prasad, Quantum limited superresolution of an incoherent source pair in three dimensions, Phys. Rev. Lett. **121**, 180504 (2018).

[36] S. M. Popoff, G. Lerosey, R. Carminati, M. Fink, A. C. Boccara, and S. Gigan, Measuring the transmission matrix in optics:

[37] P. Sebbah, R. Pnini, and A. Z. Genack, Field and intensity correlation in random media, Phys. Rev. E **62**, 7348 (2000).

[38] M. A. Webster, K. J. Webb, and A. M. Weiner, Temporal response of a random medium from third-order laser speckle frequency correlations, Phys. Rev. Lett. **88**, 033901 (2002).

[39] J. A. Newman, Q. Luo, and K. J. Webb, Imaging hidden objects with spatial speckle intensity correlations over object position, Phys. Rev. Lett. **116**, 073902 (2016).

[40] Q. Luo, J. A. Newman, and K. J. Webb, Motion-based coherent optical imaging in heavily scattering random media, Opt. Lett. **44**, 2716 (2019).

[41] A. Goetschy and A. D. Stone, Filtering random matrices: The effect of incomplete channel control in multiple scattering, Phys. Rev. Lett. **111**, 063901 (2013).

[42] Z. Shi and A. Z. Genack, Transmission eigenvalues and the bare conductance in the crossover to Anderson localization, Phys. Rev. Lett. **108**, 043901 (2012).

[43] K. A. Muttalib, J. L. Pichard, and A. D. Stone, Random-matrix theory and universal statistics for disordered quantum conductors, Phys. Rev. Lett. **59**, 2475 (1987).

[44] C. W. J. Beenakker, Random-matrix theory of quantum transport, Rev. Mod. Phys. **69**, 731 (1997).

[45] J. W. Goodman, *Speckle Phenomena in Optics: Theory and Applications* (Roberts and Company Publishers, Englewood, Colorado, 2007).

[46] J. Li and K. J. Webb, Influence of granularity on the optical properties of a negative-refractive-index lens, Phys. Rev. A **78**, 015803 (2008).

[47] J. Girard, G. Maire, H. Giovannini, A. Talneau, K. Belkebir, P. C. Chaumet, and A. Sentenac, Nanometric resolution using far-field optical tomographic microscopy in the multiple scattering regime, Phys. Rev. A **82**, 061801(R) (2010).

[48] T. Zhang, C. Godavarthi, P. C. Chaumet, G. Maire, H. Giovannini, A. Talneau, M. Allain, K. Belkebir, and A. Sentenac, Far-field diffraction microscopy at λ/10 resolution, Optica **3**, 609 (2016).

[49] S. Johnson, A. McMillan, C. Torre, S. Frick, J. Rarity, and M. Padgett, Single-pixel imaging with heralded single photons, Opt. Continuum **1**, 826 (2022).

[50] S. Farsiu, D. Robinson, M. Elad, and P. Milanfar, Advances and challenges in super-resolution, Int. J. Imaging Syst. Technol. **14**, 47 (2004).

[51] E. J. Candes, J. K. Romberg, and T. Tao, Stable signal recovery from incomplete and inaccurate measurements, Commun. Pure Appl. Math. **59**, 1207 (2006).

[52] D. L. Donoho, Compressed sensing, IEEE Trans. Inf. Theory **52**, 1289 (2006).

[53] E. J. Candes and T. Tao, Near-optimal signal recovery from random projections: Universal encoding strategies?, IEEE Trans. Inf. Theory **52**, 5406 (2006).

[54] Q. Luo, J. A. Patel, and K. J. Webb, Super-resolution sensing with a randomly scattering analyzer, Phys. Rev. Res. **3**, L042045 (2021).

[55] J. A. Patel, Q. Luo, and K. J. Webb, Eigenchannel analysis of super-resolution far-field sensing with a randomly scattering analyzer, Phys. Rev. A **107**, 023518 (2023).

[56] B. Bailey, D. L. Farkas, D. Taylor, and F. Lanni, Enhancement of axial resolution in fluorescence microscopy

by standing-wave excitation, Nature (London) **366**, 44 (1993).

[57] T. Mangeat, S. Labouesse, M. Allain, A. Negash, E. Martin, A. Guénolé, R. Poincloux, C. Estibal, A. Bouissou, S. Cantaloube, E. Vega, T. Li, C. Rouvière, S. Allart, D. Keller, V. Debarnot, X. B. Wang, G. Michaux, M. Pinot, R. Le Borgne, S. Tournier, M. Suzanne, J. Idier, and A. Sentenac, Super-resolved live-cell imaging using random illumination microscopy, Cells Rep. Methods **1**, 100009 (2021).

[58] M. Xiu, J. Field, R. Bartels, and A. Pezeshki, Fisher information and the Cramér-Rao lower bound in single-pixel localization microscopy with spatiotemporally modulated illumination, J. Opt. Soc. Am. A **40**, 185 (2023).

[59] K. J. Webb and Q. Luo, Theory of speckle intensity correlations over object position in a heavily scattering random medium, Phys. Rev. A **101**, 063827 (2020).

[60] S. Ram, E. S. Ward, and R. J. Ober, Beyond Rayleigh's criterion: A resolution measure with application to single-molecule microscopy, Proc. Natl. Acad. Sci. USA **103**, 4457 (2006).

[61] A. Classen, K. Ayyer, H. N. Chapman, R. Röhlsberger, and J. von Zanthier, Incoherent diffractive imaging via intensity correlations of hard x rays, Phys. Rev. Lett. **119**, 053401 (2017).

[62] K. Liang, S. A. Wadood, and A. N. Vamivakas, Coherence effects on estimating general sub-Rayleigh object distribution moments, Phys. Rev. A **104**, 022220 (2021).

[63] S. Divitt and A. T. Watnik, Spatial-spectral correlations of broadband speckle in around-the-corner imaging conditions, Opt. Express **30**, 7169 (2022).

[64] M. Akiba, K. Tsujino, and M. Sasaki, Ultrahigh-sensitivity single-photon detection with linear-mode silicon avalanche photodiode, Opt. Lett. **35**, 2621 (2010).

[65] B. Z. Bentz, D. Lin, and K. J. Webb, Superresolution diffuse optical imaging by localization of fluorescence, Phys. Rev. Appl. **10**, 034021 (2018).